CrystEngComm

PAPER

View Article Online
View Journal | View Issue



Cite this: *CrystEngComm*, 2019, **21**, 502

# Single crystal growth of $BaZrO_3$ from the melt at 2700 °C using optical floating zone technique and growth prospects from $BaB_2O_4$ flux at 1350 °C

Cong Xin,[abc] Philippe Veber, *[bcd] Mael Guennou, *[a] Constance Toulouse,[a] Nathalie Valle,[a] Monica Ciomaga Hatnean,[e] Geetha Balakrishnan,[e] Raphael Haumont,[f] Romuald Saint Martin,[f] Matias Velazquez,[bc] Alain Maillard,[g] Daniel Rytz,[h] Michael Josse,[bc] Mario Maglione[bc] and Jens Kreisel[ai]

Received 28th September 2018,
Accepted 10th December 2018

DOI: 10.1039/c8ce01665h

rsc.li/crystengcomm

We report the growth of $BaZrO_3$ single crystals by the optical floating zone technique and the investigation on its flux growth using $BaB_2O_4$ as a solvent. 6 mm long colorless and transparent single crystals were obtained with a mirror furnace without the need for post-treatment annealing. Its properties are determined and compared with those of two commercial crystals grown by the tri-arc Czochralski method. The chemical composition was investigated using glow discharge mass spectrometry (GDMS) and secondary ion mass spectrometry (SIMS), which indicate minor impurities of Sr, Hf, Ca and Ti, with maximal concentrations for Sr and Hf in the range of 0.3–0.5% at. The optical band gap determined by UV-visible spectroscopy is found to be ~4.8 eV and indicates the high quality of the $BaZrO_3$ crystals grown by the optical floating zone technique. Raman spectroscopy at ambient conditions and at low temperatures down to 4.2 K reveals a relatively sharp second-order spectrum and does not reveal any structural phase transition. Prospective high-temperature solution growth using $BaB_2O_4$ self-flux was investigated and led to 150–200 μm $BaZrO_3$ crystals. This solvent opens the way to grow $BaZrO_3$ at half its melting point by the flux method.



## 1. Introduction

Perovskites with general formula $ABO_3$ are an important family of multifunctional materials[1] and exhibit a broad variety of outstanding properties, which are widely used in various technological applications such as solid oxide fuel cells (SOFC),[2,3] steam electrolysis,[4] substrates for multiferroic materials,[5,6] piezoelectricity[7–13] or catalysis.[14–16] Among different perovskite compounds, barium zirconate $BaZrO_3$ (BZO) has attracted renewed interest as a high-temperature proton conductor,[17] a dielectric material for wireless communication applications,[18] a substrate for thin-film growth[19,20] and as an inert crucible for superconductors crystal growth.[21] Owing to its large lattice constant, high melting point, low thermal expansion coefficient, low dielectric loss, and low thermal conductivity,[22–24] $BaZrO_3$ has become popular for both fundamental research and device applications. More particularly, $BaZrO_3$ is known to be used in lead-free $BaTiO_3$-based (BCTZ)[25] solid solutions which exhibit high piezoelectric response,[26] whereby its role in the polarization mechanisms at the phase convergence region of this system remains poorly understood.[27] For a better understanding of the remarkable piezoelectric response of BCTZ solid solution, it is of great importance to measure the intrinsic properties[24] of $BaZrO_3$ single crystals in order to comprehend and to model more accurately $BaTiO_3$–$CaTiO_3$–$BaZrO_3$ phase diagram as previously reported.[28–30]

To the best of our knowledge, there are only a few publications available on the investigation of $BaZrO_3$ single crystal growth.[31–34] Single crystals are usually colored, small in size and their properties vary dramatically with the growth

[a] *Materials, Research and Technology Department, Luxembourg Institute of Science and Technology, University of Luxembourg, 41 Rue du Brill, 4422 Belvaux, Luxembourg. E-mail: mael.guennou@list.lu*
[b] *CNRS, ICMCB, UMR 5026, Pessac F-33600, France*
[c] *Université de Bordeaux, ICMCB, UMR 5026, Pessac F-33600, France*
[d] *Université Lyon, Université Claude Bernard Lyon 1, CNRS, Institut Lumière Matière UMR 5306, F-69100, Villeurbanne, France. E-mail: philippe.veber2@univ-lyon1.fr*
[e] *Physics Department, University of Warwick, Coventry, CV4 7AL, UK*
[f] *Institut de Chimie Moléculaire et Matériaux d'Orsay, ICMMO – UMR CNRS 8182. SP2M, Université Paris Sud, 91405 Orsay Cedex, France*
[g] *Laboratoire Matériaux Optiques Photonique et Systèmes LMOPS (EA 4423), Université de Lorraine et Centrale-Supélec, 2 rue Edouard Belin, F-57070 Metz, France*
[h] *FEE GmbH, Idar-Oberstein 55743, Germany*
[i] *Physics and Materials Science Research Unit, University of Luxembourg, 41 Rue du Brill, 4422 Belvaux, Luxembourg*

method. Because of the very high congruent melting point of $BaZrO_3$ in the range of 2500–2700 °C,[35–37] the growth of high-quality $BaZrO_3$ single crystal demands suitable techniques which avoid the contamination of single crystals by conventional container-using methods such as Czochralski and Bridgman methods. The skull-melting method has been used, but led to fractured millimeter-sized crystals featuring a strong orange color.[34]

In this work, we present the first – to the best of our knowledge – crystal growth of $BaZrO_3$ by optical floating zone and flux technique. In the former case, millimeter-sized boules grown from $BaZrO_3$ melt at 2700 °C were obtained. A (100)-oriented single crystal plate was successfully extracted and its properties were compared to those of commercial crystals with the same orientation. Chemical properties have been investigated through GDMS and SIMS. The band gap energy has been investigated by optical spectroscopy on the different single crystals. On the other hand, by using $BaB_2O_4$ flux, we were able to grow sub-millimetric single crystals at half the melting point of $BaZrO_3$. Finally, Raman spectroscopy was performed on single crystals obtained by both the flux and the optical floating zone methods. Results are discussed by comparing the data from literature and those obtained on commercial samples.

## 2. Characterization methods

Three sets of $BaZrO_3$ single crystals are characterized in this paper: i) flux grown single crystals, ii) crystals obtained with the crucible-free optical floating zone technique using a mirror furnace, labelled BZO#1, from which a (100)-oriented plate was extracted, and iii) two (100)-oriented commercial single crystals, labelled BZO#2 and BZO#3, purchased from Crystal Base Co. Ltd. and grown by tri-arc Czochralski method.

Laue back-scattering patterns were recorded using a CCD-camera device (Photonic Science dual lens coupled X-rays Laue system) after a 3–5 min stationary crystal irradiation with polychromatic X-rays supplied by a molybdenum anode. The Orientexpress software[38] was used for pattern indexing. Single crystals obtained with mirror furnace were cut along (100) direction with a diamond wire saw with an absolute accuracy less than 1°.

Exhaustive trace element chemical analysis (75 elements except C, H, O, N) was performed by glow discharge mass spectrometry (GDMS) on an as-grown single crystal grown by mirror furnace (BZO#1). GDMS model VG9000 was used with the instrumental uncertainty in between about 20% from traces (ppb wt) to 0.1 wt%. Measurements were performed under a pressure of $10^{-4}$–$10^{-5}$ mbar at liquid nitrogen temperature.

Samples BZO#1, #2, and #3 were analyzed using a CAMECA SC Ultra SIMS instrument with $O_2^+$ primary ion beam to enhance the ionization of the impurities studied. Impact energy for $O_2^+$ was 1 keV with incidence angle of 64°. A beam current of 50 nA was set over a 250 $\mu m^2$ area and ions detected from a 30 μm diameter region at the center of the crater. Analyses were performed under high vacuum conditions with chamber pressure of approximately $1 \times 10^{-8}$ mbar. They were carried out at low mass resolution. Then, the contribution of $^{48}Ca$ on mass 48 was deduced from the intensity measured for $^{40}Ca$. Samples were sputtered up to a 1 μm deep. Sputtering rate was determined by sputtering a region for an extended span of time so that the crater was sufficient to be measured despite the surface roughness. The sputtering rate obtained was 0.08 nm $s^{-1}$.

Optical transmittance of $BaZrO_3$ (100)-oriented single crystals from 200 nm to 3000 nm was recorded with a Cary 5000-UV-vis-NIR spectrometer and a resolution of 1 nm.

Micro Raman spectra were recorded in a backscattering geometry on a Renishaw inVia micro-Raman spectrometer. Two excitation laser lines were used: the 442 nm line of a He–Cd laser with an output power of 58 mW, and the 785 nm line of a Renishaw laser diode with an output power of 9 mW.

## 3. Results and discussion

### 3.1 Crystal growth by the optical floating zone technique

Feed rods were prepared with $BaZrO_3$ commercial powder (Fox-Chemicals GmbH, 99.9%) with impurity contents less than 0.006 at% for $Al_2O_3$, 0.0025 at% for $SiO_2$, 0.0021 at% for SrO, 0.008 at% for $Fe_2O_3$ and 0.007 at% for $Na_2O + K_2O$. The powder was sealed in a rubber tube and pressed under hydrostatic pressure around 50 MPa. Compacted cylindrical rods were then sintered in a horizontal furnace at 1200 °C for 24 hours under air atmosphere leading to sintered feed rods about 6.5 mm in diameter and 65 mm in length. X-ray diffraction performed on crushed pieces of sintered rods confirmed the presence of the cubic perovskite $BaZrO_3$ phase without any detectable secondary phases.

$BaZrO_3$ was grown using a four-mirror furnace equipped with xenon arc lamp (3 kW) (CSI FZ-T-12000-X_VI-VP, Crystal Systems Incorporated, Japan). The crystal growths were carried out under dynamic argon atmosphere with pressure in the range of 5–6 bar. A polycrystalline $BaZrO_3$ sintered rod was used as a seed. Once a good quality boule was obtained, a crystal seed was used for subsequent growths. The crystal boules were obtained with a growth rate of 18–25 mm $h^{-1}$. The two rods, the feed rod and the seed, were counter rotated at a rate of 5–15 rpm.

Despite the use of a high gas-pressure, a white colored deposition was observed on the quartz tube surrounding the feed rod and the seed rods, indicating the evaporation of BaO during the growth process as usually observed in zirconia-based systems[39–41] at high temperature. The as-grown $BaZrO_3$ boules were polycrystalline and mostly opaque and white colored (Fig. 1(a)) at the ends close to the seed, at the beginning of the growth. As the growth progressed, the boules produced single crystals and developed facets. Without any post-treatment annealing, as-grown single crystals are transparent to visible light, colorless and size up to 6 mm

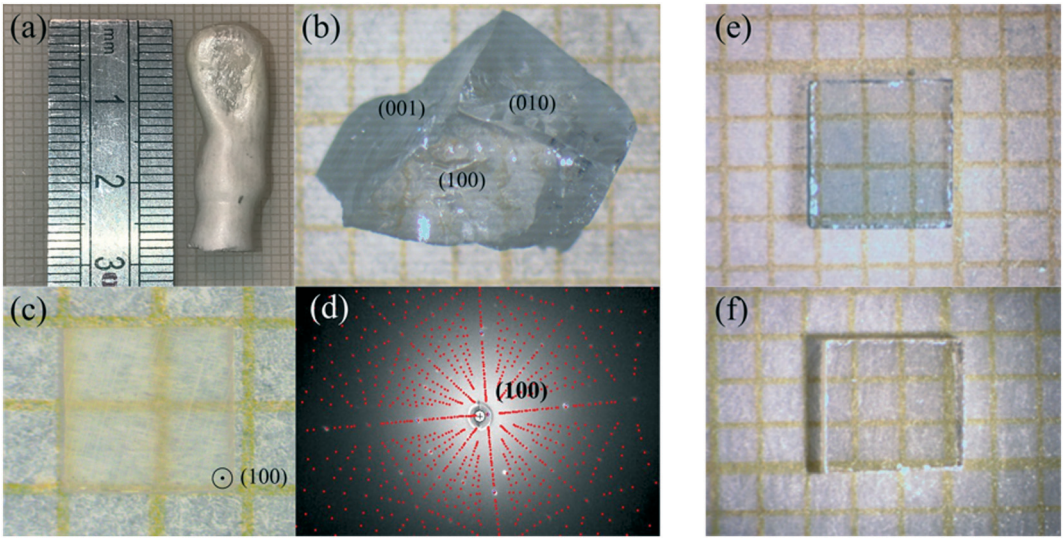


**Fig. 1** (a) Portion of a $BaZrO_3$ boule grown by the floating zone method. (b) 6 mm long $BaZrO_3$ single crystal extracted at the end of the boule. (c) Cut and (100)-oriented $BaZrO_3$ single crystal (BZO#1) ~1.99 × 1.80 × 0.6 $mm^3$ (d) back-scattered Laue diffraction pattern of $BaZrO_3$ single crystal with (100) orientation. Red dots correspond to the calculated Laue pattern. (e) BZO#2 commercial sample. (f) BZO#3 commercial sample.

long (Fig. 1(b)). A single crystal, namely BZO#1, about 1.99 × 1.80 × 0.6 $mm^3$ (Fig. 1(c)) oriented along (100) Fig. 1(d)) was extracted from the boule and optically polished for further investigations. Its properties were compared to those of two commercial samples, BZO#2 and BZO#3, (Fig. 1(e) and (f)) purchased from Crystal Base company (Japan).

### 3.2 Chemical analysis

The concentration of impurities in a 0.269 g-BZO#1 single crystal was measured by GDMS. The result of main impurities contents is summarized in Table 1. Dominant impurities in BZO#1 were found to be Ca, Sr, Ti, and Hf and belong to the IIA and IVB columns of the periodic table of the elements, like Ba and Zr, respectively. Solid solutions in between these impurities and $BaZrO_3$ are easily formed[11,25] so that they can be incorporated in the perovskite matrix with ease. On the contrary, we note that Al, Si, K and Fe impurities, as foreign elements from those of the IIA and IVB columns, present very low contents compared to those in the raw material (see 3.1).

Fig. 2 shows the secondary ion yield variations observed as a function of sputtering time $t_s$ under oxygen bombardment into $BaZrO_3$ samples BZO#1, BZO#2 and BZO#3. $t_s$ is directly proportional to the distance $z$ normal to the samples surface (about 120 nm in Fig. 2). From the results shown in Fig. 2, the intensities of most ions stabilize quite rapidly, except Ti and Ca in BZO#2 and BZO#3 single crystals. Comparison between crystals shows a higher Ca and Ti secondary ion intensity in BZO#1 than in BZO#2 and BZO#3, and an opposite trend for the Sr concentration. The prominence of Sr, Ca, Ti and Hf impurity elements observed by GDMS is thus confirmed by SIMS analysis.

The SIMS intensities are not proportional to the elemental concentrations but depend on factors like ionization yields and matrix effects. In particular, alkali and alkaline-earths ionize very easily so that Ca and Sr produce a more intense signal than Hf, even at lower concentrations. It is therefore not possible to be quantitative with SIMS alone, but we can combine SIMS with the GDMS results known for BZO#1 in order to derive the main impurity concentrations for BZO#2 and #3. Under the assumption that the concentration of the main elements Ba, Zr and O is identical between all samples (identical matrices for the three samples studied), the secondary ion intensity for impurities scales linearly with concentration. Therefore, we can use the GDMS/SIMS measurements on BZO#1 as a calibration to determine the concentrations in BZO#2 and BZO#3. Hence, we determined the concentrations for the main impurities (Hf, Sr, Ca and Ti) by rescaling their SIMS intensity with respect to the Zr intensity. The results are reported in Table 2.

Effective segregation coefficients of impurities depend on the growth rate as theoretically predicted by Burton *et al.*[42] Here, we can assume that the growth velocities in the mirror furnace (18–25 mm $h^{-1}$) are substantially larger than the pulling velocities used for Czochralski growth of oxides, which commonly range within a few mm $h^{-1}$. As experimentally referenced by Fukuda *et al.*,[43] effective segregation

**Table 1** GDMS analysis results of the impurity content in a 0.269 g BZO#1 single crystal (ppm at.)

| Element | B | Mg | Al | Si | P | S | Cl | K | Ca | Fe | Ti | Sr | Hf |
|---|---|---|---|---|---|---|---|---|---|---|---|---|---|
| BZO#1 | 0.8 | 3.4 | 6.2 | 47.3 | 1.5 | 7 | 15.6 | 4.5 | 179.4 | 1.3 | 370 | 1420 | 3001 |

 

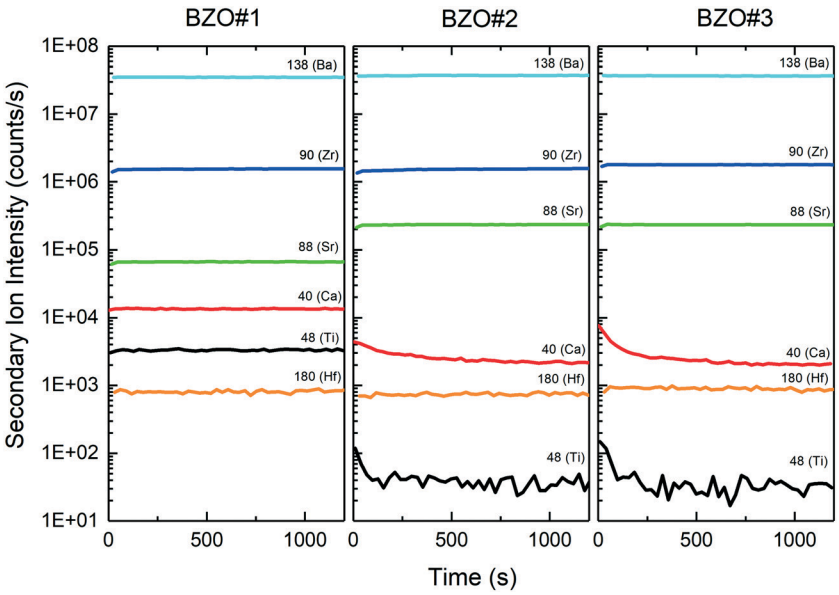


Fig. 2 SIMS depth profile (raw data) analysis of all samples.

coefficients tend to be 1 for high pulling speeds. They are usually lower than 1 for foreign ions,[42] so that impurities are rejected at the liquid–solid interface during the growth and their contents increase progressively into the liquid during the growth. In the present work, owing to the high pulling velocity employed, impurities with effective segregation coefficient lower than 1 have been incorporated in a larger amount within the crystal grown with a mirror furnace than those grown in a tri-arc Czochralski furnace. On the contrary, impurities with effective segregation coefficients higher than 1, are incorporated in a lower amount with the mirror furnace grown crystal. Considering that the raw materials are of the same minimum purity (3 N), we can reasonably conclude that the effective segregation coefficient of Sr in the A site of $BaZrO_3$ perovskite is higher than 1, similarly to what can be deduced from the sign of the solidus and liquidus curves of the $BaTiO_3$–$SrTiO_3$ perovskite system.[44] In the same way, effective segregation coefficients of Hf, Ca and Ti are lower than 1, as previously referenced for Ca and Ti in $BaZrO_3$-based perovskite solid solutions.[45]

### 3.3 Physical properties

**3.3.1 Optical properties.** Fig. 3 shows the transmittance of the three samples BZO#1, #2 and #3. $BaZrO_3$ single crystals are essentially transparent in the visible and NIR regions and exhibit a sharp absorption edge in the near-UV. BZO#2 is remarkably different from the other crystals in that it exhibits a strong absorption band in the lower part of the visible spectrum, with a main peak around 800 nm, which is consistent with the blueish color of the crystal (see photo Fig. 1(e)). This blueish color and the absorption band can likely be attributed to differences in oxygen stoichiometry, as previously shown for example on $La_{0.5}Na_{0.5}TiO_3$.[46]

Table 2 Summary of the main impurity contents (ppm at) for the three single crystals derived from GDMS and SIMS measurements

| | Hf | Sr | Ca | Ti |
|---|---|---|---|---|
| BZO#1 | 3001 | 1420 | 179 | 370 |
| BZO#2 | 2791 | 5157 | 32 | 4 |
| BZO#3 | 2937 | 4426 | 28 | 3 |

$BaZrO_3$ is expected to have an indirect gap according to most electronic structure calculations reported in the literature,[47–50] with a conduction band minimum at the $\Gamma$ point (0,0,0) and a valence band maximum at the $R$ point (1/2, 1/2, 1/2), where the phonon energies can be as high as 100 meV.[24,51] These computations also suggest a relatively flat valence band, with a local maximum at $\Gamma$ only 250 meV lower than the absolute maximum, where direct transitions would be allowed. One study even reports a direct band gap at $\Gamma$.[52]

Experimentally, the nature and the value of the band gap can in principle be determined by the Tauc plot, *i.e.* plotting $(\alpha{\cdot}h\nu)^{1/r}$ as the function of the energy $h\nu$, where $\alpha$ is the absorption coefficient and $r$ equals 1/2 or 2 for, respectively, a direct or indirect gap. The absorption can be determined from the transmittance $T$, reflectivity $R$, and thickness d of the samples using the relation $T \approx (1-R)^2\exp(-\alpha d)$.[53] We neglect reflectivity in the following. The absorption edge is expected to exhibit a linear regime for $r$ = 1/2 or $r$ = 2, depending on the character of the gap. Fig. 3(b) and (c) show the Tauc plots for the three crystals, whereby the blueish BZO#2 appears very different from the two others. Colorless BZO#1 and BZO#3 exhibit a linear region in both plots, and extrapolations of this linear region gives gap values that are very similar for the two samples: 4.89/4.86 eV for $r$ = 1/2 (hypothesis of the direct gap) and 4.76/4.74 eV for $r$ = 2 (hypothesis of the indirect band gap) for BZO#1/#3 respectively. Those

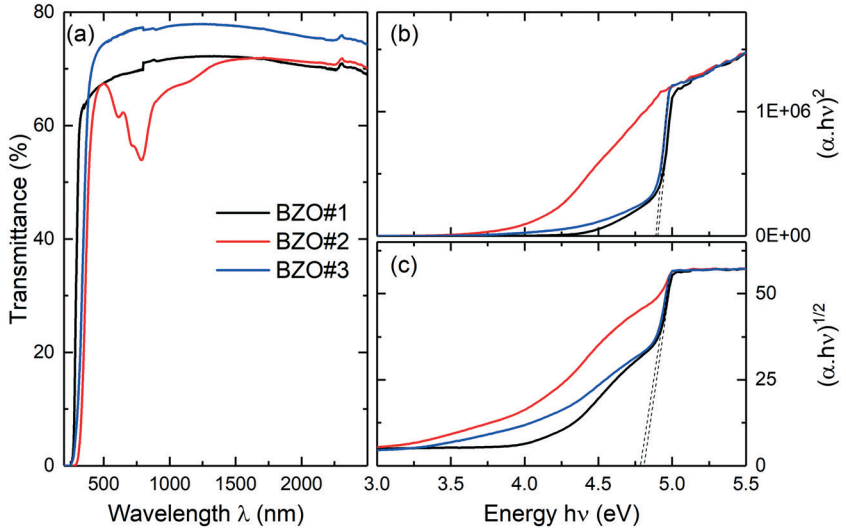


**Fig. 3** (a) Optical transmission spectra of $BaZrO_3$ single crystal of BZO#1, BZO#2, BZO#3 in a wide wavelength range. (b) and (c) Tauc plots with, respectively, $r = 1/2$ and $r = 2$.

values, consistent between the two samples and very close to each other, seem to confirm the indirect character of the gap, but also the existence of direct transitions allowed at a hardly higher energy, as suggested by computations. In addition, both crystals show a pronounced Urbach tail linked to near-edge defects states. In BZO#2, this appears so dominant that no linear region can be identified.

In the present work, the value of ~4.8 eV matches the 4.1–4.8 eV reported in a study of $BaZrO_3$ powders prepared with various degrees of disorder,[49] and the 5.0 eV found on a similar study with powder prepared by solid state reactions.[54] On the other hand, it is much higher than the 3.8 eV reported in[55] a study of powders obtained by the sol–gel route. As commonly observed, many computations underestimate the band gap value (3.2 eV in ref. 48, 50 and 56).

**3.3.2 Raman spectroscopy analysis.** $BaZrO_3$ is cubic with the space group $Pm\bar{3}m$ and has no first-order Raman-active phonon mode. In spite of this, an intense Raman spectrum is usually observed,[31,57,58] in a way that is reminiscent of other cubic perovskites ($SrTiO_3$,[59] $KTaO_3$ (ref. 60)). Second-order scattering processes involving combinations of two phonons usually explains it.

Fig. 4(a) shows the Raman spectra of BZO#1, BZO#2 and BZO#3 single crystals measured at ambient conditions in parallel scattering geometry. The spectra present a comparable signature, which are similar in their main features to the few spectra reported in the literature.[31,57,61] Raman spectra were collected upon cooling down to 4.2 K (Fig. 4(b)). The comparison of the spectra at low and room temperatures does not show any indication for a phase transition. Slight changes, such as a subtle sharpening of the bands, very small shifts in their positions, or the general weakening of the low frequency bands can all be attributed to thermal effects. The emergence of a couple of very weak and thin peaks can be noticed, but have to be attributed to extrinsic effects and defects. This is demonstrated by the observation that they are found at different positions in BZO#1 grown in the present work and in the commercial BZO#2 and BZO#3 samples. Such spurious Raman lines are not uncommon in perovskites,[62] but cannot be assigned conclusively here.

### 3.4 Investigation on $BaZrO_3$ growth with $BaB_2O_4$ as a potential flux

The flux method from high temperature solution is investigated in order to decrease the crystallization temperature of $BaZrO_3$. As suggested by the $BaTiO_3$–$BaB_2O_4$ phase diagram referenced by Goto *et al.*[63] and because B ions cannot be

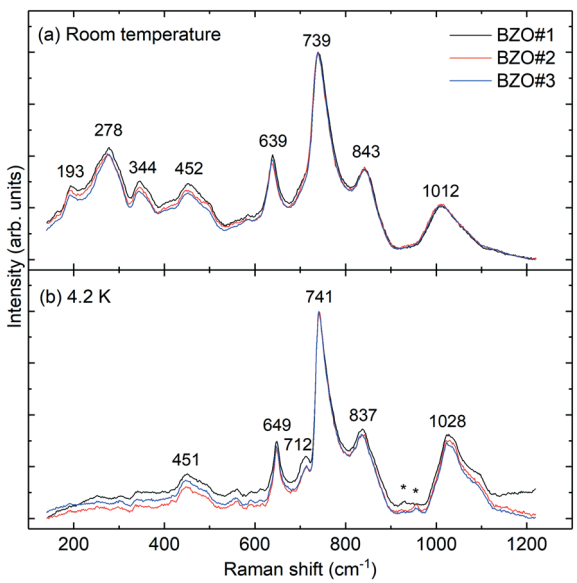


**Fig. 4** Raman scattering spectra of $BaZrO_3$ single crystals measured with a 442 nm excitation at (a) ambient temperatures and (b) at 4.2 K. The positions of the main peaks are indicated. The stars mark the weak lines emerging at low temperature, as discussed in the text.

 

inserted into the $BaTiO_3$ lattice as a foreign element, $BaB_2O_4$ (BBO) could be used as a suitable self-flux[19] to grow $BaTiO_3$ at temperatures as low as 942 °C, which is more than 650 °C below the $BaTiO_3$ melting point ($T_f$ = 1618 °C). Although the detailed $BaZrO_3$–BBO phase diagram is unknown, we assumed that the $BaZrO_3$–BBO system exhibits the same phase diagram feature than that of $BaTiO_3$–BBO because of the chemical similarity of $Ti^{4+}$ and $Zr^{4+}$ cations. Therefore, $BaZrO_3$ : BBO mixtures were investigated for different molar ratios such as 10 : 90, 20 : 80, 30 : 70, 35 : 65, 40 : 60 and 50 : 50, in order to characterize the solubility of $BaZrO_3$ in BBO. The BBO flux was prepared by solid state reaction[64] by mixing $BaCO_3$ (Alfa Aesar, 99.95%) and $B_2O_3$ (Alfa Aesar, 99.98%). Then, BBO was mixed with $BaZrO_3$ commercial powder (Fox-Chemicals GmbH, 99.9%). 10 g ball-milled mixtures were placed into a platinum crucible tightly covered with a platinum lid and placed in a large alumina crucible. A two-heating-resistive-zone furnace was used to achieve a 1 °C $cm^{-1}$ longitudinal thermal gradient. The process was performed in the following steps: i) an increasing temperature ramp of 120 °C $h^{-1}$ up to 1350 °C, with a 1-hour dwelling time at this temperature, ii) a decreasing ramp with 1 °C $h^{-1}$ down to 1250 °C, and finally, iii) the mixtures were cooled down at a rate of 30 °C $h^{-1}$ down to room temperature. The mass of the crucible containing the mixtures was monitored all along the thermal process.

In all cases, a strong volatilization as well as flux creeping outside of the crucible were observed with a loss of approximatively one half of the total weight of the loads.

In the lower-$BaZrO_3$-content solutions corresponding to 10 : 90, 20 : 80 and 30 : 70 $BaZrO_3$–BBO mixtures, no $BaZrO_3$ crystallites were detected. In the particular case of 10 : 90 $BaZrO_3$–BBO solution, millimeter-sized yellow single crystals (Fig. 5(a)), with (111)-natural facets (Fig. 5(b)) corresponding to rhombohedral $BaZr(BO_3)_2$ (BZB) phase, were extracted from the solidified solution.

Higher-$BaZrO_3$-content solutions corresponding to 35 : 65, 40 : 60 and 50 : 50 $BaZrO_3$–BBO mixtures displayed two solidified zones with white and brown colors (Fig. 5(c)). In the brown zone, $BaZrO_3$ single crystals were successfully obtained (Table 3) and their structure has been confirmed by single crystal XRD with space group $Pm\bar{3}m$ and $a$ = 4.18 Å.

The largest $BaZrO_3$ crystals that can show a rectangular-like face with a size up to 150–200 μm (Fig. 5(d)) were found in the brown zone from the 35 : 65 $BaZrO_3$–BBO solution where yellow BZB micrometric crystals with triangle-like shape are also detected. Crystallites with micrometric-sized were detected in 40 : 60 and 50 : 50 $BaZrO_3$–BBO solutions.

XRD diffractograms (Fig. 6) display $BaZrO_3$, $Ba_2B_2O_5$ and BZB phases in both white and brown zones with a higher proportion of $BaZrO_3$ in the brown zone where rectangular single crystals were detected and collected. Micro-Raman spectroscopy was performed on the as-grown crystals from the 35 : 65 $BaZrO_3$–BBO solution (Fig. 7). Crystals with large flat facets exhibit a spectrum that matches previously reported Raman spectra of $BaZrO_3$ (ref. 31, 57 and 61) as well as the spectra shown in Fig. 4. Finally, as we obtained only BZO, BZB and $Ba_2B_2O_5$ phases in the brown zone where, respectively, their structures are cubic (ICDD No. 006-0399), rhombohedral

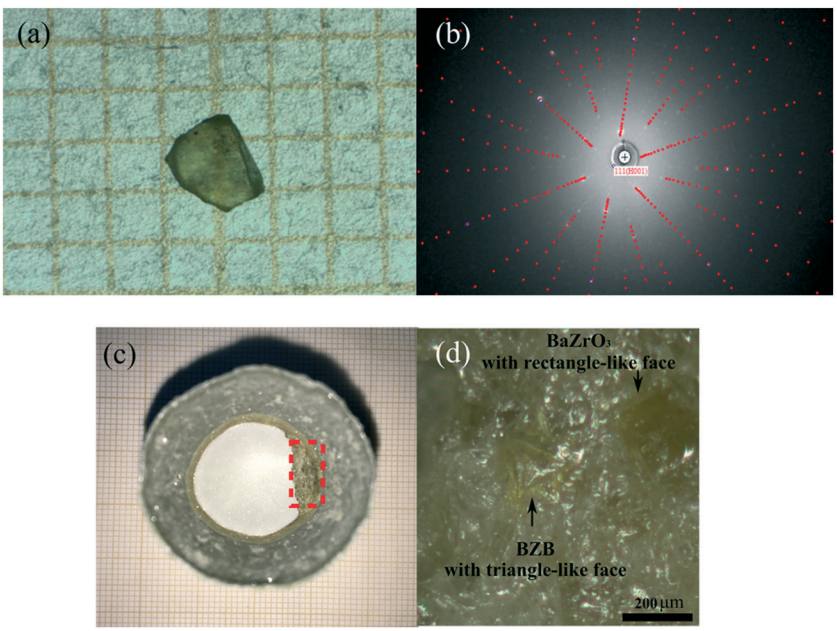


**Fig. 5** Flux growth with 35 : 65 $BaZrO_3$–BBO solution: (a) $BaZr(BO_3)_2$ (BZB) single crystals grown from 10 : 90 $BaZrO_3$–BBO solution with (b) (111)-natural faces highlighted in a Laue pattern (red dots correspond to theoretical pattern whereas white dots correspond to experimental pattern). (111) rhombohedral faces correspond to (001) hexagonal face, noted (H001). (c) Crucible containing the 35 : 65 $BaZrO_3$–BBO solution exhibiting the BBO flux (white zone) and the BZO crystals (brown zone). (d) Zoom on BZO single crystals (brown zone) with a rectangle-like shape. A yellow BZB crystal with a triangle-like shape is detected.

**Table 3** Mixtures of $BaZrO_3$–$BaB_2O_4$ with different molar ratio together with the typical size of BZO crystals grown in the tightly lid-covered crucible

| Mixture $BaZrO_3$ : BBO (mol%) | Presence of BZO | BZO crystals typical size |
|---|---|---|
| 10 : 90 | × | × |
| 20 : 80 | × | × |
| 30 : 70 | × | × |
| 35 : 65 | ✓ | ~150 μm |
| 40 : 60 | ✓ | ~10 μm |
| 50 : 50 | ✓ | ~10 μm |

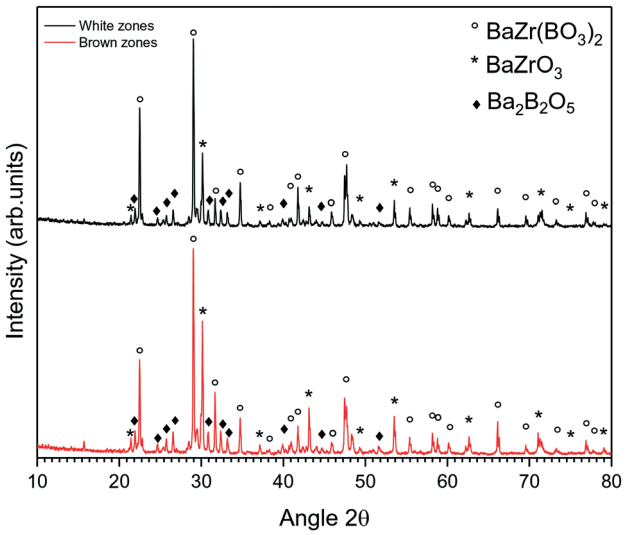


**Fig. 6** XRD patterns of crushed sample extracted from the brown zone (red pattern) and the white zone (black patterns) obtained from the flux growth attempt into a tightly lid-covered platinum crucible with 35 : 65 BZO–BBO solution.

(ICDD No. 056-0239) and monoclinic (ICDD No. 024-0087), it is worth noticing that crystals with natural rectangular faces observed on Fig. 1b features typically the habit of crystals belonging to orthogonal coordinate systems, so that brown rectangular single crystal shown in Fig. 5(d) can only correspond to cubic $BaZrO_3$. In the same way, yellow triangular crystal shown in Fig. 5(d) corresponds to rhombohedral BZB.

The spectrum of BZB[61] was also confirmed, consistently with the XRD analysis. Some additional spectral features are observed but cannot not be conclusively identified. In particular, they do not match the Raman spectrum expected from the BBO flux[56] or $ZrO_2$.[65] We may tentatively attribute it to the $Ba_2B_2O_5$ detected in XRD, but no reference Raman spectrum is available in the literature to confirm this hypothesis. We conclude that a chemical reaction occurs between BZO and BBO, which leads to the formation of BZB and $Ba_2B_2O_5$ at 1350 °C, and it is described by the following equation:

$$2BaB_2O_4 + BaZrO_3 \xrightarrow{1350\,^{\circ}C} BaZr(BO_3)_2 + Ba_2B_2O_5$$

Furthermore, in an attempt to increase the crystal size by avoiding the flux creeping and its volatilization from the solution, a crystal growth was performed with $BaZrO_3$–BBO 35 : 65 molar ratio under controlled atmosphere in a sealed and gas-proof platinum assembly for saturating the vapor pressure as previously reported by Albino *et al.*[66] The same thermal protocol was performed as above-mentioned. After thermal process, XRD analysis revealed the presence of $BaZrO_3$, BBO and BZB compounds in the solidified solution (see insert of Fig. 8) without any $BaZrO_3$ single crystal visible under a microscope (×64). This confirms that the use of a sealed atmosphere prevents the decomposition of BBO into $Ba_2B_2O_5$ but not the formation of BZB, and this points out that the solubility of $BaZrO_3$ in BBO is very low and below the XRD detection limit. In addition, this highlights that the flux volatilization was the driving force governing the growth of $BaZrO_3$ obtained in the tightly lid-covered crucible.

Finally, we noted that the formation of BZB is systematically observed, whatever the platinum assembly used. The chemical reaction in between BBO and $BaZrO_3$ decreases the amount of the latter in the BBO-based solution, partly impeding then its growth at 1350 °C. Hence, a growth attempt was performed with BZB as a self-flux with $BaZrO_3$–BZB 50 : 50 molar ratio. BZB was synthesized by solid state reaction[67] and mixed to $BaZrO_3$ commercial powder. The load was held in an open iridium crucible under argon atmosphere for 12 h at a temperature in a 1550–1640 °C range, as determined through pyrometric measurement. A strong volatilization of the solution was observed, prohibiting the growth of $BaZrO_3$ single crystal from BZB flux. Indeed, XRD analysis (Fig. 9)

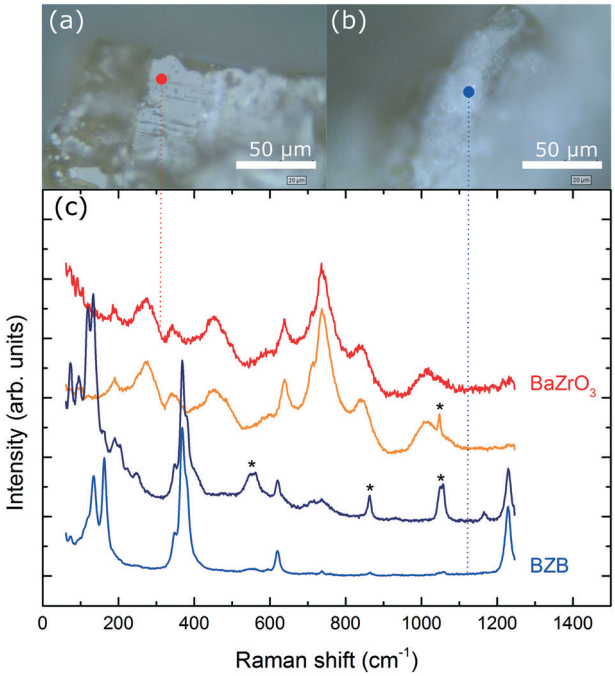


**Fig. 7** Selected Raman spectra recorded in different parts of the flux grown crystals with a 785 nm excitation line. (a) and (b) Show two representative spots where the spectra of $BaZrO_3$ and BZB can be observed as indicated in (c), together with other spectra showing mixed cases and Raman bands (marked with a star) that are tentatively assigned to $Ba_2B_2O_5$.

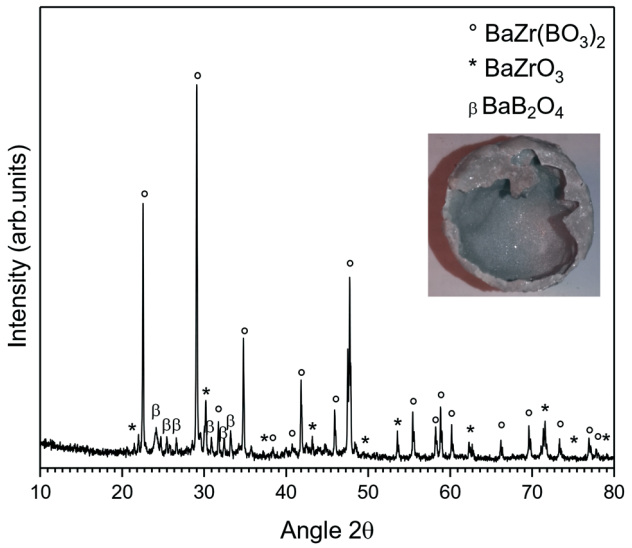


Fig. 8 XRD pattern of crushed sample from the flux growth attempt into a sealed platinum crucible with 35 : 65 BZO–BBO solution. In insert: view of the load after the thermal process. No crystal was detected.

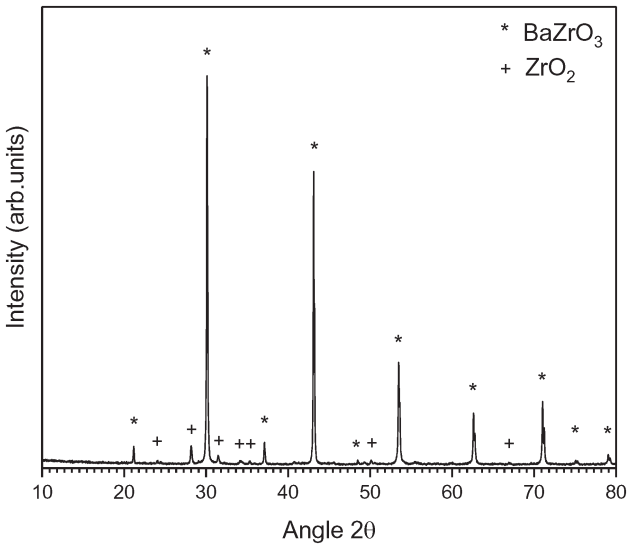


Fig. 9 XRD pattern of crushed sample from the flux growth attempt into an open iridium crucible with 50 : 50 BZB–BZO solution.

revealed the presence of only $BaZrO_3$ and $ZrO_2$ phases resulting likely from the decomposition of BZB at high temperature. We infer that the high thermal chemical stability of $BaZrO_3$ makes it difficult to dissolve in the investigated Ba-based flux of the present work.

## 4. Conclusion

The growth of $BaZrO_3$ by the optical floating zone technique and its investigation by the flux method are reported for the first time. $BaZrO_3$ boules have been successfully grown by optical floating zone technique with single crystal sizes up to 6 mm long. They are transparent, colorless and have been shaped as millimeter-sized plate oriented along (100) direction. Four dominant elements that can make easily solid solutions with $BaZrO_3$ were observed through GDMS and SIMS analysis: Ca, Ti, Sr and Hf, whereas other foreign elements contents are drastically decreased compared to their initial content in the raw material. This highlights that optical floating zone method is a suitable technique for removing foreign impurities from oxide crystals contrary to oxide crystals classically grown with a highly polluting environment, such as refractory ceramics and metallic crucibles, inducing a higher impurities contents with the same or a higher raw material purity.[68–70] Optical measurements performed on $BaZrO_3$ single crystal exhibit a high optical band gap energy of ~4.8 eV, most probably indirect, although direct electronic transitions are only slightly higher in energy. Raman study revealed a second-order spectrum, with sharp features. This Raman spectrum does not change significantly down to the lowest temperature measured (4.2 K). The availability of large single crystals opens the possibility for fundamental studies of $BaZrO_3$, notably its dynamics at the macroscopic and local scales.

Finally, the flux method using $BaB_2O_4$ solvent enables to grow 150–200 μm-sized single crystals at half the melting point (1350 °C) of $BaZrO_3$. Crystals size and quality are restricted by the formation of $BaZr(BO_3)_3$, which has been revealed by Raman spectroscopy and XRD diffraction. While it is demonstrated that $BaZrO_3$ solubility is poor in $BaB_2O_4$ flux, this self-flux growth approach makes possible to crystallize this highly refractory material at low temperatures.

## Conflicts of interest

There are no conflicts to declare.

## Acknowledgements

The authors would like to thank Dr Stanislas Pechev and M Alexandre Fargues for, respectively, $BaZrO_3$ single crystal XRD and optical transmission analysis performed at ICMCB. This work was supported by the Innovative Training Networks (ITN) – Marie Skłodowska-Curie Actions-European Joint Doctorate in Functional Material Research (EJD-FunMat) project (no. 641640). The work at the University of Warwick was supported by the EPSRC, UK, Grant EP/M028771/1. Cong Xin, Dr. Mael Guennou, Dr Constance Toulouse and Prof. Jens Kreisel acknowledge support from the National Research Fund Luxembourg through a Pearl Grant (FNR/P12/4853155).

## References

1 R. H. Mitchell, *Perovskites: modern and ancient*, Almaz Press Thunder Bay, 2002, vol. 7.
2 S. Tao and J. T. S. Irvine, A redox-stable efficient anode for solid-oxide fuel cells, *Nat. Mater.*, 2003, **2**, 320.
3 Y.-H. Huang, R. I. Dass, Z.-L. Xing and J. B. Goodenough, Double perovskites as anode materials for solid-oxide fuel cells, *Science*, 2006, **312**(5771), 254–257.

4 G. Tsekouras, D. Neagu and J. T. S. Irvine, Step-change in high temperature steam electrolysis performance of perovskite oxide cathodes with exsolution of B-site dopants, *Energy Environ. Sci.*, 2013, **6**(1), 256–266.
5 J. Wang, J. Neaton, H. Zheng, V. Nagarajan, S. Ogale, B. Liu, D. Viehland, V. Vaithyanathan, D. Schlom and U. Waghmare, Epitaxial $BiFeO_3$ multiferroic thin film heterostructures, *Science*, 2003, **299**(5613), 1719–1722.
6 R. Ramesh and N. A. Spaldin, Multiferroics: progress and prospects in thin films, in *Nanoscience And Technology: A Collection of Reviews from Nature Journals*, World Scientific, 2010, pp. 20–28.
7 H. Liu, P. Veber, J. Rödel, D. Rytz, P. B. Fabritchnyi, M. I. Afanasov, E. A. Patterson, T. Frömling, M. Maglione and J. Koruza, High-performance piezoelectric (K,Na,Li)(Nb,Ta,Sb)$O_3$ single crystals by oxygen annealing, *Acta Mater.*, 2018, **148**, 499–507.
8 P. Veber, F. Benabdallah, H. Liu, G. Buse, M. Josse and M. Maglione, Growth and characterization of lead-free piezoelectric single crystals, *Materials*, 2015, **8**(11), 7962–7978.
9 F. Benabdallah, P. Veber, M. Prakasam, O. Viraphong, K. Shimamura and M. Maglione, Continuous cross-over from ferroelectric to relaxor state and piezoelectric properties of $BaTiO_3$-$BaZrO_3$-$CaTiO_3$ single crystals, *J. Appl. Phys.*, 2014, **115**(14), 144102.
10 H. Liu, P. Veber, J. Koruza, D. Rytz, M. Josse, J. Rödel and M. Maglione, Influence of $Ta^{5+}$ content on the crystallographic structure and electrical properties of $[001]_{PC}$-oriented (Li,Na,K)(Nb,Ta)$O_3$ single crystals, *CrystEngComm*, 2016, **18**(12), 2081–2088.
11 J. Rödel, W. Jo, K. T. P. Seifert, E.-M. Anton, T. Granzow and D. Damjanovic, Perspective on the development of lead-free piezoceramics, *J. Am. Ceram. Soc.*, 2009, **92**(6), 1153–1177.
12 Y. Saito, H. Takao, T. Tani, T. Nonoyama, K. Takatori, T. Homma, T. Nagaya and M. Nakamura, Lead-free piezoceramics, *Nature*, 2004, **432**(7013), 84.
13 H. Liu, J. Koruza, P. Veber, D. Rytz, M. Maglione and J. Rödel, Orientation-dependent electromechanical properties of Mn-doped (Li,Na,K)(Nb,Ta)$O_3$ single crystals, *Appl. Phys. Lett.*, 2016, **109**(15), 152902.
14 K. Maeda and K. Domen, Water oxidation using a particulate $BaZrO_3$-$BaTaO_2N$ solid-solution photocatalyst that operates under a wide range of visible light, *Angew. Chem., Int. Ed.*, 2012, **51**(39), 9865–9869.
15 G. Tsekouras and J. T. S. Irvine, The role of defect chemistry in strontium titanates utilised for high temperature steam electrolysis, *J. Mater. Chem.*, 2011, **21**(25), 9367–9376.
16 J. Varghese, R. W. Whatmore and J. D. Holmes, Ferroelectric nanoparticles, wires and tubes: synthesis, characterisation and applications, *J. Mater. Chem. C*, 2013, **1**(15), 2618–2638.
17 K. D. Kreuer, Proton-Conducting Oxides, *Annu. Rev. Mater. Res.*, 2003, **33**(1), 333–359.
18 M. T. Sebastian, *Dielectric materials for wireless communication*, Elsevier, 2010.
19 A.-M. Azad, S. Subramaniam and T. W. Dung, On the development of high density barium metazirconate ($BaZrO_3$) ceramics, *J. Alloys Compd.*, 2002, **334**(1), 118–130.
20 P. S. Dobal, A. Dixit, R. S. Katiyar, Z. Yu, R. Guo and A. S. Bhalla, Micro-Raman scattering and dielectric investigations of phase transition behavior in the $BaTiO_3$–$BaZrO_3$ system, *J. Appl. Phys.*, 2001, **89**(12), 8085–8091.
21 E. Celik, Y. Akin, I. H. Mutlu, W. Sigmund and Y. S. Hascicek, $BaZrO_3$ insulation coatings for HTS coils, *Phys. C*, 2002, **382**(4), 355–360.
22 R. Vassen, X. Cao, F. Tietz, D. Basu and D. Stöver, Zirconates as new materials for thermal barrier coatings, *J. Am. Ceram. Soc.*, 2000, **83**(8), 2023–2028.
23 P. K. Davies, J. Tong and T. Negas, Effect of ordering-induced domain boundaries on low-loss $Ba(Zn_{1/3}Ta_{2/3})O_3$-$BaZrO_3$ perovskite microwave dielectrics, *J. Am. Ceram. Soc.*, 1997, **80**(7), 1727–1740.
24 A. Akbarzadeh, I. Kornev, C. Malibert, L. Bellaiche and J. Kiat, Combined theoretical and experimental study of the low-temperature properties of $BaZrO_3$, *Phys. Rev. B: Condens. Matter Mater. Phys.*, 2005, **72**(20), 205104.
25 M. Acosta, N. Novak, V. Rojas, S. Patel, R. Vaish, J. Koruza, G. A. Rossetti Jr. and J. Rödel, $BaTiO_3$-based piezoelectrics: Fundamentals, current status, and perspectives, *Appl. Phys. Rev.*, 2017, **4**(4), 041305.
26 W. Liu and X. Ren, Large piezoelectric effect in Pb-free ceramics, *Phys. Rev. Lett.*, 2009, **103**(25), 257602.
27 D. S. Keeble, F. Benabdallah, P. A. Thomas, M. Maglione and J. Kreisel, Revised structural phase diagram of $(Ba_{0.7}Ca_{0.3}TiO_3)$-$(BaZr_{0.2}Ti_{0.8}O_3)$, *Appl. Phys. Lett.*, 2013, **102**(9), 092903.
28 D. Amoroso, A. Cano and P. Ghosez, First-principles study of (Ba,Ca)$TiO_3$ and Ba(Ti,Zr)$O_3$ solid solutions, *Phys. Rev. B*, 2018, **97**(17), 174108.
29 Y. Nahas, A. Akbarzadeh, S. Prokhorenko, S. Prosandeev, R. Walter, I. Kornev, J. Íñiguez and L. Bellaiche, Microscopic origins of the large piezoelectricity of leadfree (Ba,Ca)(Zr,Ti)$O_3$, *Nat. Commun.*, 2017, **8**, 15944.
30 T. Yang, X. Ke and Y. Wang, Mechanisms Responsible for the Large Piezoelectricity at the Tetragonal-Orthorhombic Phase Boundary of $(1\text{-}x)BaZr_{0.2}Ti_{0.8}O_3$-$xBa_{0.7}Ca_{0.3}TiO_3$ System, *Sci. Rep.*, 2016, **6**, 33392.
31 M. A. Helal, T. Mori and S. Kojima, Terahertz time-domain spectroscopy and Raman scattering studies of incipient ferroelectric $BaZrO_3$, *Ferroelectrics*, 2016, **499**(1), 107–114.
32 M. Helal, T. Mori and S. Kojima, Softening of infrared-active mode of perovskite $BaZrO_3$ proved by terahertz time-domain spectroscopy, *Appl. Phys. Lett.*, 2015, **106**(18), 182904.
33 A. V. Babinskii, V. A. Trepakov, N. N. Krainik, B. A. Melekh, G. A. Smolenskii, A. A. Andreev and M. M. Kazanin, Growth and thermoluminescence of $BaZrO_3$ single crystals, *Soviet Technical Physics Letters.*, 1977, **3**(11), 477–478.
34 M. S. Paun, *Single crystal growth of high melting oxide materials by means of induction skull melting*, 2015.
35 W. P. Gong, T. F. Chen and Z. P. Jin, Thermodynamic investigation of $ZrO_2$-BaO system, *Trans. Nonferrous Met. Soc. China*, 2007, **17**(2), 232–237.

 

36 J. O. A. Paschol, H. Kleykamp and F. Thümmler, Phase equilibria in the pseudoquaternary BaO-$UO_2$-$ZrO_2$-$MoO_2$ system, *J. Nucl. Mater.*, 1987, **151**(1), 10–21.
37 A. Shevchenko, Reactions in the system $HfO_2$-SrO, $HfO_2$-BaO, and $ZrO_2$-BaO in high $HfO_2$ or $ZrO_2$ regions, *Inorg. Mater.*, 1987, **23**(9), 1322.
38 B. Ouladdiaf, J. Archer, G. McIntyre, A. Hewat, D. Brau and S. York, OrientExpress: A new system for Laue neutron diffraction, *Phys. B*, 2006, **385**, 1052–1054.
39 N. S. Jacobson, *Thermodynamic properties of some metal oxide-zirconia systems*, National aeronautics and space administration cleveland oh lewis research center, 1989.
40 J. Fisher, D.-H. Kim, S. Lee, D. Nguyen and J.-S. Lee, Reactive sintering of BaY0.1Zr0.9O3-δ proton conducting ceramics with CuO liquid phase sintering aid, *J. Ceram. Process. Res.*, 2013, **14**, 703–706.
41 M. D. Gonçalves, P. S. Maram, R. Muccillo and A. Navrotsky, Enthalpy of formation and thermodynamic insights into yttrium doped $BaZrO_3$, *J. Mater. Chem. A*, 2014, **2**(42), 17840–17847.
42 J. Burton, R. Prim and W. Slichter, The distribution of solute in crystals grown from the melt. Part I. Theoretical, *J. Chem. Phys.*, 1953, **21**(11), 1987–1991.
43 T. Fukuda and H. Hirano, Solid-solution $LiTa_xNb_{1-x}O_3$ single crystal growth by Czochralski and edge-defined film-fed growth technique, *J. Cryst. Growth*, 1976, **35**(2), 127–132.
44 J. A. Basmajian and R. C. Devries, Phase Equilibria in the System $BaTiO_3$–$SrTiO_3$, *J. Am. Ceram. Soc.*, 1957, **40**(11), 373–376.
45 G. Buse, C. Xin, P. Marchet, A. Borta-Boyon, M. Pham-Thi, H. Cabane, E. Veron, M. Josse, M. Velazquez, M. Lahaye, E. Lebraud, M. Maglione and P. Veber, Spinodal decomposition in lead-free piezoelectric $BaTiO_3$–$CaTiO_3$–$BaZrO_3$ crystals, *Cryst. Growth Des.*, 2018, **18**(10), 5874–5884.
46 R. Haumont, R. Saint-Martin, J. Chaigneau, M. Devant, J. Hermet, B. Neela Sekhar, Y. Uesu, M. Itoh and J. M. Kiat, Growth of quantum paraelectric $La_{1/2}Na_{1/2}TiO_3$ single crystals using optical floating zone technique, *J. Cryst. Growth*, 2011, **321**(1), 36–39.
47 L. S. Kouchaksaraie, Theoretical calculation of electrical and optical properties of $BaZrO_3$, *International Journal of Mathematical, Computational, Physical, Electrical and Computer Engineering*, 2011, **5**(11), 1680–1683, World Academy of Science, Engineering and Technology.
48 X. Yang, Y. Wang, Q. Song, Y. Chen and Y. H. Xue, Pressure effects on structural, electronic, elastic, and optical properties of cubic and tetragonal phases of $BaZrO_3$, *Acta Phys. Pol., A*, 2018, **133**(5), 1138–1143.
49 L. S. Cavalcante, J. C. Sczancoski, V. M. Longo, F. S. De Vicente, J. R. Sambrano, A. T. de Figueiredo, C. J. Dalmaschio, M. S. Li, J. A. Varela and E. Longo, Intense violet–blue photoluminescence in $BaZrO_3$ powders: A theoretical and experimental investigation of structural order–disorder, *Opt. Commun.*, 2008, **281**(14), 3715–3720.
50 R. Terki, H. Feraoun, G. Bertrand and H. Aourag, Full potential calculation of structural, elastic and electronic properties of $BaZrO_3$ and $SrZrO_3$, *Phys. Status Solidi B*, 2005, **242**(5), 1054–1062.
51 J. W. Bennett, I. Grinberg and A. M. Rappe, Effect of symmetry lowering on the dielectric response of $BaZrO_3$, *Phys. Rev. B: Condens. Matter Mater. Phys.*, 2006, **73**(18), 180102.
52 S. M. Alay-e-Abbas, S. Nazir and A. Shaukat, Formation energies and electronic structure of intrinsic vacancy defects and oxygen vacancy clustering in $BaZrO_3$, *Phys. Chem. Chem. Phys.*, 2016, **18**(34), 23737–23745.
53 R. Bhatt, I. Bhaumik, S. Ganesamoorthy, A. Karnal, M. Swami, H. Patel and P. Gupta, Urbach tail and bandgap analysis in near stoichiometric LiNbO3 crystals, *Phys. Status Solidi A*, 2012, **209**(1), 176–180.
54 H. Volkova, *Ferroelectric perovskite oxides for photovoltaics and photocatalysis*, MINES, ParisTech, 2018.
55 S. Lee, R. D. Levi, W. Qu, S. C. Lee and C. A. Randall, Band-gap nonlinearity in perovskite structured solid solutions, *J. Appl. Phys.*, 2010, **107**(2), 023523.
56 J.-L. You, G.-C. Jiang, H.-Y. Hou, Y.-Q. Wu, H. Chen and K.-D. Xu, Temperature-dependent Raman spectra and microstructure of barium metaborate crystals and its melts, *Chin. Phys. Lett.*, 2002, **19**(2), 205.
57 C. Chemarin, N. Rosman, T. Pagnier and G. Lucazeau, A high-pressure Raman study of mixed perovskites $BaCe_xZr_{1-x}O_3$ $(0 \leq x \leq 1)$, *J. Solid State Chem.*, 2000, **149**(2), 298–307.
58 P. Colomban and A. Slodczyk, Raman intensity: an important tool in the study of nanomaterials and nanostructures, *Acta Phys. Pol., A*, 2009, **116**(1), 7.
59 W. Nilsen and J. Skinner, Raman spectrum of strontium titanate, *J. Chem. Phys.*, 1968, **48**(5), 2240–2248.
60 W. Nilsen and J. Skinner, Raman spectrum of potassium tantalate, *J. Chem. Phys.*, 1967, **47**(4), 1413–1418.
61 M. Mączka, K. Szymborska-Małek, A. Gągor and A. Majchrowski, Growth and characterization of acentric $BaHf(BO_3)_2$ and $BaZr(BO_3)_2$, *J. Solid State Chem.*, 2015, **225**, 330–334.
62 S. Saha, B.-C. Cao, M. Motapothula, C.-X. Cong, T. Sarkar, A. Srivastava, S. Sarkar, A. Patra, S. Ghosh, Ariando, J. M. D. Coey, T. Yu and T. Venkatesan, Magnetic modes in rare earth perovskites: A magnetic-field-dependent inelastic light scattering study, *Sci. Rep.*, 2016, **6**, 36859.
63 Y. Goto and L. Cross, Phase diagram of the $BaTiO_3$-$BaB_2O_4$ system and growth of $BaTiO_3$ crystals in the melt, *Yogyo Kyokaishi*, 1969, **77**(11), 355–357.
64 L. Deyra, A. Maillard, R. Maillard, D. Sangla, F. Salin, F. Balembois, A. Kokh and P. Georges, Impact of $BaB_2O_4$ growth method on frequency conversion to the deep ultra-violet, *Solid State Sci.*, 2015, **50**, 97–100.
65 M. Ishigame and T. Sakurai, Temperature dependence of the Raman spectra of $ZrO_2$, *J. Am. Ceram. Soc.*, 1977, **60**(7–8), 367–369.
66 M. Albino, P. Veber, E. Castel, M. Velázquez, K. Schenk, G. Chapuis, M. Lahaye, S. Pechev, M. Maglione and M. Josse, Growth and characterization of centimeter-sized

$Ba_2LaFeNb_4O_{15}$ crystals from high-temperature solution under a controlled atmosphere, *Eur. J. Inorg. Chem.*, 2013, **2013**(15), 2817–2825.

67 V. Hornebecq, P. Gravereau, J. P. Chaminade and E. Lebraud, $BaZr(BO_3)_2$: a non-centrosymmetric dolomite-type superstructure, *Mater. Res. Bull.*, 2002, **37**(13), 2165–2178.

68 M. Velázquez, P. Veber, G. Buşe, Y. Petit, P. Goldner, V. Jubera, D. Rytz, A. Jaffres, M. Peltz, V. Wesemann, P. Aschehough and G. Aka, Spectroscopic properties of newly flux grown and highly $Yb^{3+}$-doped cubic $RE_2O_3$ (RE=Y, Gd, Lu) laser crystals, *Opt. Mater.*, 2015, **39**, 258–264.

69 P. Veber, M. Velázquez, G. Gadret, D. Rytz, M. Peltz and R. Decourt, Flux growth at 1230 °C of cubic $Tb_2O_3$ single crystals and characterization of their optical and magnetic properties, *CrystEngComm*, 2015, **17**(3), 492–497.

70 P. Veber, M. Velázquez, V. Jubera, S. Péchev and O. Viraphong, Flux growth of $Yb^{3+}$-doped $RE_2O_3$ (RE=Y, Lu) single crystals at half their melting point temperature, *CrystEngComm*, 2011, **13**(16), 5220–5225.

 